2

Theoretical aspects of spin transport in graphene and carbon nanotubes

Abstract

In this chapter I present the physics behind electrical spin injection and detection in a nonmagnetic material. I discuss the conventional spin valve device and introduce the non-local spin transport technique. I develop a model for spin transport in a nonmagnetic material which takes into account conductivity mismatch. I present and discuss the spin relaxation mechanisms which can be found in a nonmagnetic material. I conclude with a number of basic electronic and spintronic properties of graphene and of single-wall carbon nanotubes.

2.1 Spin injection and detection

In this section I describe the mechanism of electrical spin injection and detection in a nonmagnetic material. A description of the conventional two probe spin valve and the non-local four probe technique is given. A very valuable method to extract the spin relaxation time in a nonmagnetic material is by performing a spin precession experiment. For this I develop a model taking into account spin relaxation, diffusion and precession in a spin valve device. I conclude with a short description and discussion of possible spin relaxation mechanisms.

2.1.1 All electrical spin injection and detection

A current which moves through a diffusive conductor can be considered to be carried in parallel by two independent spin channels, a channel for the spin up electrons and one for the spin down electrons [1]. This holds when most scattering events preserve the spin orientation, otherwise the two channels become strongly coupled and are not independent anymore. The spin current density $j_{\uparrow,\downarrow}$ of the spin up $\uparrow$ or spin down $\downarrow$ channel is proportional to the gradient of the electrochemical potential of one of the two spin species and is given by the relation:

$$j_{\uparrow,\downarrow} = \frac{\sigma_{\uparrow,\downarrow}\partial\mu_{\uparrow,\downarrow}}{e\partial x} \tag{2.1}$$

where $\sigma_{\uparrow,\downarrow}$ is the conductivity, $\mu_{\uparrow,\downarrow}$ the chemical potential of the two spin channels and e is the electron charge. The total charge current is given by $\mathrm{j} = j_\uparrow + j_\downarrow$ and the spin current j_s is given by $\mathrm{j}_s = j_\uparrow - j_\downarrow$. Looking now into a ferromagnet in which $\sigma_\uparrow \neq \sigma_\downarrow$ we can define a spin polarization p given by the relation:

$$p = \frac{j_\uparrow - j_\downarrow}{j_\uparrow + j_\downarrow} = \frac{\sigma_\uparrow - \sigma_\downarrow}{\sigma_\uparrow + \sigma_\downarrow} \tag{2.2}$$

using $\sigma_\uparrow + \sigma_\downarrow = \sigma$ which is the total conductivity in the system we obtain:

$$p = \frac{\sigma_\uparrow - \sigma_\downarrow}{\sigma} \tag{2.3}$$

and equation 2.1 becomes

$$j_\uparrow = (1+p)\frac{\sigma\partial\mu_\uparrow}{2e\partial x} \tag{2.4}$$

$$j_\downarrow = (1-p)\frac{\sigma\partial\mu_\downarrow}{2e\partial x} \tag{2.5}$$

We can use the ferromagnet as a spin source because $j_\uparrow \neq j_\downarrow$. In practice, ferromagnets are used in conventional two-terminal spin valve devices. A spin

valve device contains two ferromagnetic electrodes, the injector and the detector, which make contact to a nonmagnetic material. Sending an electrical current through the ferromagnetic injector creates a spin accumulation in the nonmagnetic material. In a diffusive material this accumulation decays exponentially with distance from the spin injector following the differential equation:

$$\frac{\partial^2 \Delta\mu}{\partial x^2} = \frac{\Delta\mu}{\lambda_{sf}^2} \tag{2.6}$$

where $\lambda_{sf} = \sqrt{D\tau_{sf}}$ is the spin relaxation length, D the diffusion constant, τ_{sf} the spin relaxation time and $\Delta\mu = \mu_\uparrow - \mu_\downarrow$. If the spins relax fast, such as to reach a uniform distribution over spin direction before arriving at the spin injector, then the spin detector measures the average chemical potential which is zero. In this case, switching the magnetization of the ferromagnets from parallel to antiparallel gives no change in the total resistance of the spin valve. However, in the situation in which the detector is set within a distance λ_{sf} from the spin injector, a switching of the magnetization of the ferromagnets from parallel to antiparallel produces a change in the spin valve resistance. The reason for this is that when the magnetization of injector and detector are parallel, the spins can enter easily the spin detector, corresponding to a low resistance of the spin valve. However, when the magnetization of the detector is antiparallel to the injector then the spins first have to flip their magnetization before they can enter the detector, this results to an increase in resistance.

2.1.2 Spin injection and detection, the non-local technique

The conventional two-terminal spin valve geometry can be used to extract the spin relaxation length, λ_{sf}. Unfortunately, in this geometry, it is sometimes difficult to separate spin transport from other effects, such as Hall effects, anisotropic magnetoresistance [2, 3], interference effects [4], and magneto-coulomb effects [5]. These effects may obscure or even mimic the spin accumulation signal. With a four-terminal non-local spin valve geometry [2, 6, 7], one is able to completely separate the spin current path from the charge current path. Hence, the signal measured is due to spin transport only.

To determine spin accumulation in the non-local geometry, one needs to contact the system under investigation (metal, semiconductor, carbon nanotube) with four electrodes. At least two of these should be ferromagnetic. They act as spin injector and spin detector, respectively. For practical reasons, we make use of devices in which all contacts are ferromagnetic (Fig. 2.1 a). These electrodes are narrow, but of different widths to assure different switching fields B_C [2, 7]. As shown in Fig. 2.1 two of the ferromagnetic electrodes are connected to a current

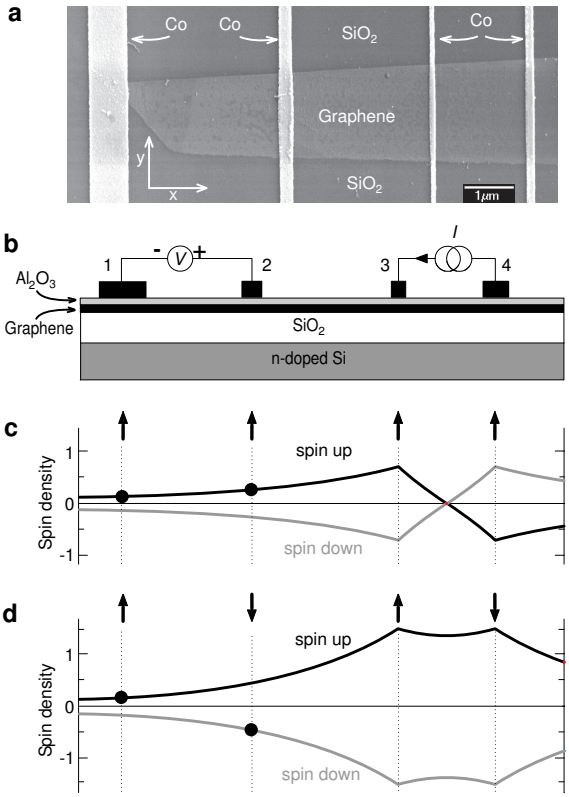

Figure 2.1: Spin transport in a four terminal graphene based spin valve device. a, scanning electron microscope micrograph of a four terminal single layer graphene spin valve. Cobalt electrodes are evaporated across a single layer graphene strip prepared on a SiO_2 surface. b, The non-local spin valve geometry: A current I is injected from electrode 3 through the Al_2O_3 barrier into graphene and is extracted at contact 4. The voltage difference is measured between contact 2 and 1. The non-local resistance is: $R_{non-local}$=(V_+-V_-)/I. c, Illustration of spin injection and spin diffusion for electrodes having parallel magnetizations. Injection of up spins by contact 3 results in an accumulation of spin-up electrons underneath contact 3, with a corresponding deficit of spin-down electrons. Due to spin relaxation the spin density decays on a scale given by the spin relaxation length. The dots show the electric voltage measured by contact 1 and 2 in the ideal case of 100% spin selectivity. A positive non-local resistance is measured. d, Spin injection and spin diffusion for antiparallel magnetizations. The voltage contacts probe opposite spin directions resulting in a negative non-local resistance.

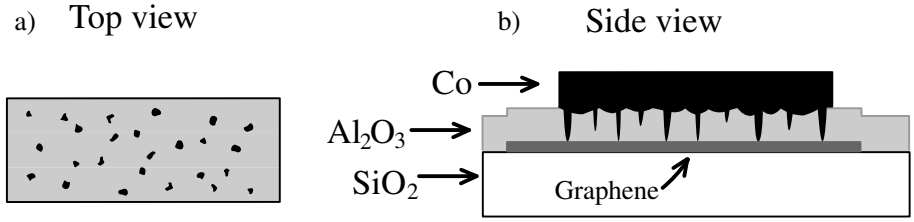

Figure 2.2: Cartoon illustrating the type of contact between a ferromagnetic electrode (cobalt) and a graphene layer separated by an Al_2O_3 layer. a) Top view showing an Al_2O_3 layer containing pinholes filled with cobalt. b) Side view. A cobalt electrode making contact to the graphene layer.

source, such that a charge current flows into a small part of the nonmagnetic material. The material in this case is a single layer of graphene. To be able to inject and detect spins dynamics in the system, it is necessary to use tunnel barriers (for example Al_2O_3) between the ferromagnetic electrodes and the graphene layer underneath, in order to increase the spin-dependent interface resistance, and combat the conductivity mismatch problem [8]. In practice we do not obtain an uniform tunnel barrier since the contact resistance between the cobalt electrode and the graphene flake shows no clear tunneling behavior. The precise nature of contact is unknown, probably the Al_2O_3 contains pinholes filled with ferromagnetic cobalt which provide an electrical link between the ferromagnetic electrode and the graphene layer (Fig. 2.2). Also, it is essential for the device to have contacts opaque enough so that carriers can pass underneath it with conservation of spin direction. Since we use ferromagnetic electrodes the current is spin-polarized and results in the creation of spin accumulation inside the graphene layer. These spin-polarized electrons will diffuse in the graphene and if they conserve their spin until they reach the voltage contacts, a voltage will be measured. Therefore, if spin injection and spin transport take place, a bipolar spin signal should be observed which changes sign when the magnetization configuration of the spin injector and detector switches from parallel to anti-parallel (Fig. 2.3). Due to the absence of a background resistance, the non-local technique is less sensitive to device resistance fluctuations and spurious magnetoresistances (such as Hall effects), as compared to the standard two-terminal spin valve technique.

2.1.3 Spin precession and conductivity mismatch

In the non-local geometry but also in the conventional geometry, the effectiveness of spin injection and detection strongly depends on the relative magnitude of the contact resistance of the ferromagnetic electrodes compared to the resistance of

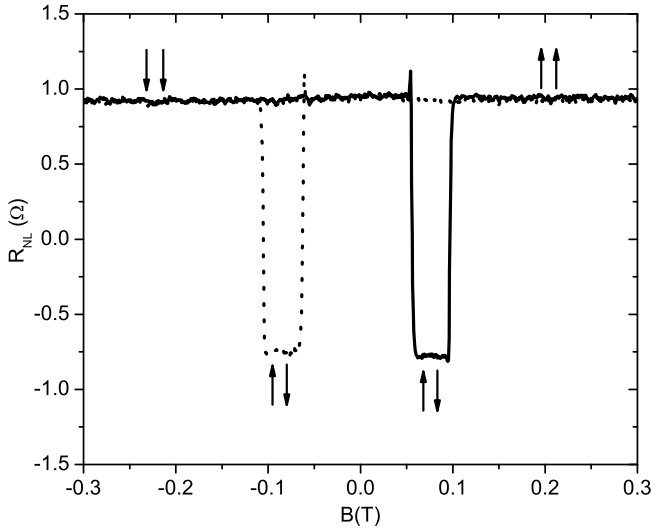

Figure 2.3: Example of a non-local measurement performed on the nonmagnetic material graphene (measurement performed on sample B in chapter 7). The observed resistance switching is due to spin accumulation and spin transport in graphene. The distance between the spin injector and the detector is 2 μm. The non-local resistance R_{NL} is negative when the spin injector is magnetized antiparallel to the spin detector. In this situation the detector measures mainly the negative chemical potential of the spin down species. The solid line is a magnetic trace to the right and the dotted line to the left.

the nonmagnetic material. A small contact resistance with respect to the nonmagnetic material, unavoidably, results in the so-called conductivity mismatch and also provides an extra path for spin relaxation at the ferromagnetic contacts [8]. This has to be taken into account in fitting of the spin precession measurements by solving the 1-dimensional Bloch equations [7]. The Bloch equations describe the combined effect of diffusion, precession and spin relaxation in the system:

$$D\frac{d^2\vec{\mu}}{dx^2} - \frac{\vec{\mu}}{\tau} + \frac{g\mu_B}{\hbar}(\vec{B} \times \vec{\mu}) = 0 \tag{2.7}$$

Where D is the diffusion constant, μ is the chemical potential of the spin species, τ is the spin relaxation time, g is the g-factor, B the magnetic field, $\hbar$ is Planck's constant and μ_B the Bohr magneton. Replacing $\frac{g\mu_B}{\hbar}\vec{B}$ with $\vec{\omega}_L$ simplifies the above equation to:

$$D\frac{d^2\vec{\mu}}{dx^2} - \frac{\vec{\mu}}{\tau} + \vec{\omega}_L \times \vec{\mu} = 0 \tag{2.8}$$

To perform these Hanle type spin precession experiments we first apply a magnetic field in the y-direction (Fig. 2.1), along the long axis of the ferromagnets, to prepare the magnetizations of the electrodes in a parallel or antiparallel orientation. Then this field is removed and a B-field in the z-direction is scanned. An example of spin precession is depicted in Fig. 2.4, in the case of parallel ($\uparrow\uparrow$, black curve) and antiparallel ($\uparrow\downarrow$, grey curve) magnetizations of the spin injector and spin detector cobalt electrodes. Spins parallel to the graphene plane precess while they are diffusing towards the spin detector at a distance $L = 4$ μm from the injector. At B$\sim$0.2 T their average precession angle when they arrive at this contact is 180 degrees, resulting in a sign reversal of the spin signal. To extract the diffusion constant D and relaxation time τ we have to solve the Bloch equations (eq. 2.8).

As described above, we apply a magnetic field in the z-direction, therefore B = B$_z$ (B$_x$ = B$_y$ = 0) and equation 2.8 becomes:

$$D\frac{d^2}{dx^2}\begin{pmatrix}\mu_x\\ \mu_y\\ \mu_z\end{pmatrix} - \frac{1}{\tau}\begin{pmatrix}\mu_x\\ \mu_y\\ \mu_z\end{pmatrix} + \omega_L\begin{pmatrix}\mu_y\\ -\mu_x\\ 0\end{pmatrix} = 0 \tag{2.9}$$

The solutions of the above equation are:
For the z direction:

$$\begin{pmatrix}\mu_x\\ \mu_y\\ \mu_z\end{pmatrix} = \begin{pmatrix}0\\ 0\\ 1\end{pmatrix}\exp(\mp K_1 x), K_1 = \frac{1}{\lambda_{sf}} = \frac{1}{\sqrt{D\tau}} \tag{2.10}$$

To find the solutions in the x and y direction, we assume

$$\begin{pmatrix}\mu_x\\ \mu_y\end{pmatrix} = \begin{pmatrix}\mu_{x0}\\ \mu_{y0}\end{pmatrix}\exp(-K_2 x) \tag{2.11}$$

Then the Bloch equations in x,y become:

$$DK_2^2\begin{pmatrix}\mu_{x0}\\ \mu_{y0}\end{pmatrix} - \frac{1}{\tau}\begin{pmatrix}\mu_{x0}\\ \mu_{y0}\end{pmatrix} + \omega_L\begin{pmatrix}\mu_{y0}\\ -\mu_{x0}\end{pmatrix} = 0 \tag{2.12}$$

This can be written in matrix form:

$$\begin{pmatrix}Dk_2^2 - \frac{1}{\tau} & \omega_L\\ -\omega_L & Dk_2^2 - \frac{1}{\tau}\end{pmatrix}\begin{pmatrix}\mu_{x0}\\ \mu_{y0}\end{pmatrix} = 0 \tag{2.13}$$

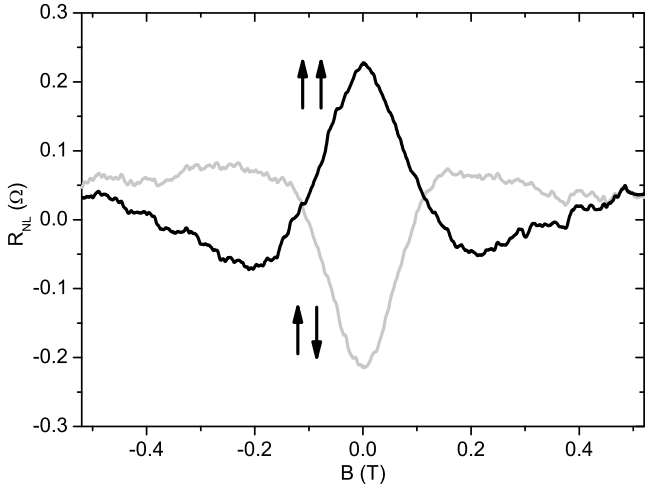

Figure 2.4: Hanle type spin precession experiment performed on a graphene layer (see chapter 7). Spin precession in case of parallel (↑↑, black curve) and antiparallel (↑↓, grey curve) magnetizations of spin injector and detector. Spins precess while they travel from the injector towards the detector at a distance of 4 μm. At B$\sim$0.2 T their average precession angle when they arrive at this contact is 180 degrees, resulting in a sign reversal of the spin signal.

Finding the determinant $(DK_2^2 - \frac{1}{\tau})^2 + \omega_L^2 = 0$ results in

$$K_2 = \pm\sqrt{\frac{1}{D\tau} \pm \frac{i\omega_L}{D}} \tag{2.14}$$

The eigenvectors are:

$$\begin{pmatrix}\mu_{x0}\\ \mu_{y0}\end{pmatrix} = \begin{pmatrix}1\\ -i\end{pmatrix}\exp(\pm K_2^+), K_2^+ = \sqrt{\frac{1}{D\tau} + \frac{i\omega_L}{D}} \tag{2.15}$$

and

$$\begin{pmatrix}\mu_{x0}\\ \mu_{y0}\end{pmatrix} = \begin{pmatrix}1\\ i\end{pmatrix}\exp(\pm K_2^-), K_2^- = \sqrt{\frac{1}{D\tau} - \frac{i\omega_L}{D}} \tag{2.16}$$

Now we have the following system (Fig. 2.5): a spin injector electrode at x = 0 and a spin detector electrode at x = L. In practice the two electrodes, which are ferromagnetic, induce extra spin relaxation into the system. This relaxation

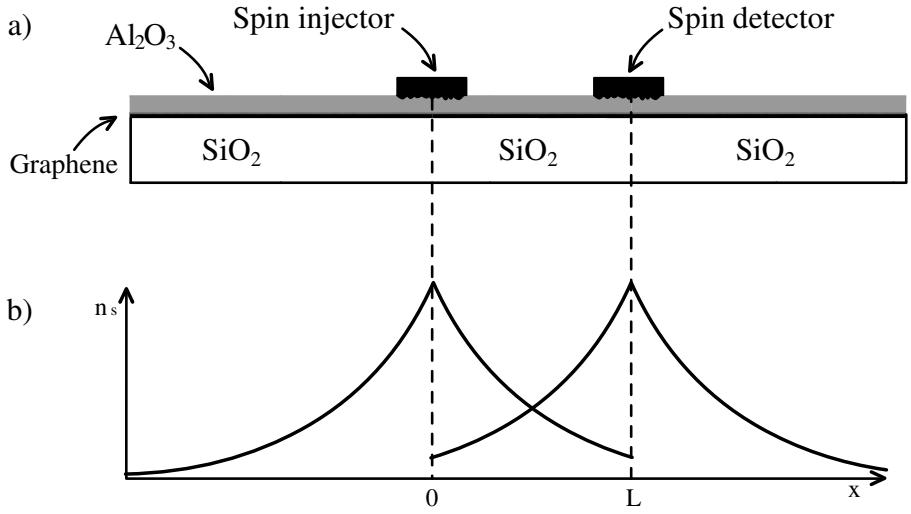

Figure 2.5: Cartoon illustrating a) a ferromagnetic electrode injecting spins in a graphene layer and a ferromagnetic electrode used to detect spins b) The contacts induce extra spin scattering in the system. Result is that in order to calculate the spin density in the system, we have to take into account exponential functions not only on both sides of the spin injector but also on both sides of the spin detector.

is taken into account in the model by introducing a parameter R which describes the relative importance of spin relaxation at the contacts. The precise definition of R will be given in the next section.

At the left side of the spin injector (thus for x $\leq$ 0), the dependency of the spin signal is given by the sum of the three following terms:

$$\begin{pmatrix}\mu_x\\ \mu_y\\ \mu_z\end{pmatrix} = j\begin{pmatrix}0\\0\\1\end{pmatrix}\exp(K_1 x) + k\begin{pmatrix}1\\-i\\0\end{pmatrix}\exp(K_2^+ x) + l\begin{pmatrix}1\\i\\0\end{pmatrix}\exp(K_2^- x) \qquad (2.17)$$

Between the injector and detector (0$\leq$ x $\leq$L) we search for a solution build by the following terms:

$$\begin{aligned} &a\begin{pmatrix}0\\0\\1\end{pmatrix}\exp(-K_1 x) + b\begin{pmatrix}1\\-i\\0\end{pmatrix}\exp(-K_2^+ x) + c\begin{pmatrix}1\\i\\0\end{pmatrix}\exp(-K_2^- x)\\ &+d\begin{pmatrix}0\\0\\1\end{pmatrix}\exp(K_1 x) + e\begin{pmatrix}1\\-i\\0\end{pmatrix}\exp(K_2^+ x) + f\begin{pmatrix}1\\i\\0\end{pmatrix}\exp(K_2^- x)\end{aligned} \qquad (2.18)$$

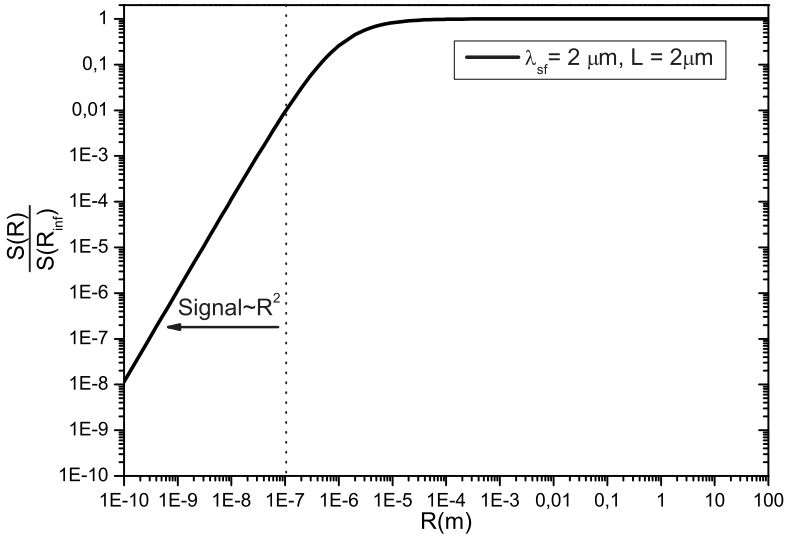

Figure 2.6: Influence of the contact on the measured spin signal when L = 2 μm and λ_{sf} = 2 μm. The normalized spin signal S(R)/S(R_∞) has a quadratic dependence in R for $R << 10^{-5}$m. At large R the signal S(R) saturates to the spin signal found at R_∞, clearly, the contacts to do not influence the spin signal. Note that the threshold value $R = 10^{-5}$m is defined by λ_{sf} (see text).

And for x≥L:

$$g\begin{pmatrix}0\\0\\1\end{pmatrix}\exp(-K_1x)+h\begin{pmatrix}1\\-i\\0\end{pmatrix}\exp(-K_2^+x)+i\begin{pmatrix}1\\i\\0\end{pmatrix}\exp(-K_2^-x) \tag{2.19}$$

We need to find the 12 unknowns (prefactors a to l). The boundary conditions necessary to solve the problem are: a) continuity of μ_x, μ_y and μ_z at x = 0 and x = L. b) continuity of the first derivative (spin currents) at x = 0 and x = L. Continuity of μ_x, μ_y and μ_z at x = 0 results in (x, y and z component):

$$\begin{aligned}(x)&: k+l=b+c+e+f\\(y)&: -k+l=-b+c-e+f\\(z)&: a+d=j\end{aligned} \tag{2.20}$$

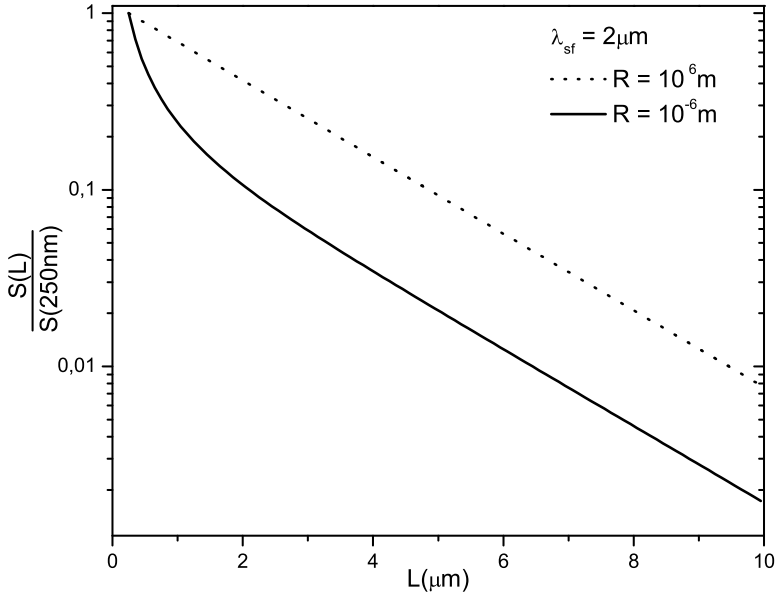

Figure 2.7: Dependence of the (normalized) spin signal S(L)/S(250nm) as function of L for $R = 10^6 m$ and $R = 10^{-6} m$. Here we used $\lambda_{sf} = 2$ μm. An exp(-L/λ_{sf}) dependence in the spin signal is found for $R = 10^6 m$, clearly no spin relaxation happens at the contacts. In the case of spin relaxation at the contacts ($R = 10^{-6} m$) we obtain a $1/L$ dependence in the spin signal for L<λ_{sf}. At higher values of L the signal returns to the exponential dependence in L, however with reduced amplitude.

Continuity at x = L results in:

$$\begin{aligned}
&(x) : be^{-K_2^+ L} + ce^{-K_2^- L} + ee^{K_2^+ L} + fe^{K_2^- L} = he^{-K_2^+ L} + ie^{-K_2^- L} \\
&(y) : -be^{-K_2^+ L} + ce^{-K_2^- L} - ee^{K_2^+ L} + fe^{K_2^- L} = -he^{-K_2^+ L} + ie^{-K_2^- L} \\
&(z) : ae^{-K_1 L} + de^{K_1 L} = ge^{-K_1 L}
\end{aligned} \tag{2.21}$$

Continuity of the first derivative means continuity in spin currents. We only send a spin current in the x-direction, therefore we have I = $I_x(0)$, $I_y(0) = 0$ and $I_z(0) = 0$. Solving for example for $I_z(0) = 0$ at x = 0 we obtain:

$$K_1 j + K_1 a - K_1 d + \frac{\mu_z(0)}{R} = 0, \mu_z(0) = j \tag{2.22}$$

where $\frac{\mu_z(0)}{R}$ is the spin current which relaxes back to the ferromagnetic contact. R is equal to $R_c W/R_{sq}$ (see next section, equation 2.34), where R_c is the resistance of the contact, R_{sq} the resistance of the nonmagnetic material and W the width of the nonmagnetic material. Similar conditions as eq. 2.22 can be found for $I_y(0) = 0$:

$$K_2^+ k + K_2^- l - K_2^+ b + K_2^- c + K_2^+ e - K_2^- f + \frac{-k+l}{R} = 0 \tag{2.23}$$

and for $I_x(0) = I$:

$$K_2^+ k + K_2^- l + K_2^+ b + K_2^- c - K_2^+ e - K_2^- f + \frac{k+l}{R} = I \tag{2.24}$$

Three more equations are obtained at x = L. A total of 12 equations with 12 unknowns are defined and can be solved using a program like MatLab. Input parameters in this model are R, L, D and τ. In Fig. 2.6 we plot the spin signal normalized to the value of the spin signal at R$\rightarrow \infty$ as function of the parameter R. The parameters L, D and τ are set to be constant (L = 2μm, $\lambda_{sf} = \sqrt{D\tau} =$ 2μm). When $R << 10^{-5} m$ we find a signal which has a quadratic dependence in R. For $R >> 10^{-5} m$ the normalized signal saturates to the value 1 since no spin relaxation is induced at the contacts. Note that the value of R at which this crossover happens is proportional to λ_{sf}. Close investigation of eq. 2.22 shows that this is indeed the case, the value of R has to be proportional to λ_{sf} since K_1 is proportional to $1/\lambda_{sf}$.

In Fig. 2.7 we show how the spin signal changes as function of electrode spacing L for two different values of R (=10^{-6} m, 10^6 m). At $R = 10^{-6}$ m and for $L < \lambda_{sf}$ we obtain a $1/L$ dependence in the spin signal (M. Popinciuc *et al*, in preparation). This dependency is characteristic for a system in which the contacts induce spin relaxation and it clearly differs from the exp(-L/λ_{sf}) dependence found at large values of R (no relaxation). The model developed in this sector has been used to fit the data of spin precession in graphene in Chapter 7. Here a conductivity mismatch problem arises due to the fact that the contact resistance R_c between the cobalt electrode and the graphene layer covered by a thin layer of Al_2O_3 is equal or smaller to the typical square resistance of the graphene layer R_{sq}.

2.1.4 Definition of the R value

The above model needs to be modified in such a way that it produces a quantitative value of the chemical potential of the spins at a certain distance from the spin injector. For this we need to find the value R.

First step is to represent a contact which is spin polarized and induces spin relaxation in the system with its equivalent resistor model. This model is depicted

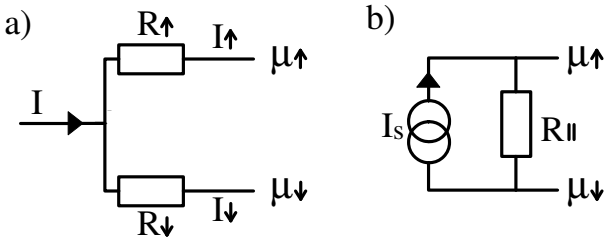

Figure 2.8: Resistor model of the contact. a) A current I passes through a spin dependent contact having a resistance $R_\uparrow$ for the spin up channel and $R_\downarrow$ for the spin down channel. This current is distributed along the two channels in such a way that $I_\uparrow + I_\downarrow = I$. At the output of the contact we have a difference in chemical potential $\Delta\mu = \mu_\uparrow$ - $\mu_\downarrow$ b) The equivalent current source of the contact in a), with $I_s = \frac{R_\downarrow - R_\uparrow}{R_\uparrow + R_\downarrow} I$ and $R_{||} = R_\uparrow + R_\downarrow$.

in Fig. 2.8 a). A current I is distributed along two spin channels, a spin current I↑ passes through a resistance $R_\uparrow$ in the spin up (↑) channel and a spin current I↓ through $R_\downarrow$ in the spin down (↓) channel. The current I is given by:

$$I = I_\uparrow + I_\downarrow \tag{2.25}$$

The total spin current I_s is given by:

$$I_s = I_\uparrow - I_\downarrow \tag{2.26}$$

This model can be further simplified by representing it with a current source having a resistance $R_\parallel$ in parallel (Fig. 2.8 b). The spin current which the source produces, I_s, can be found by the resistor model in Fig. 2.8 a) (we set $\mu_\uparrow$ - $\mu_\downarrow$ = 0), from this we obtain $I_\uparrow$ and $I_\downarrow$:

$$I_\uparrow = \frac{R_\downarrow}{R_\uparrow + R_\downarrow} I \tag{2.27}$$

$$I_\downarrow = \frac{R_\uparrow}{R_\uparrow + R_\downarrow} I \tag{2.28}$$

Using equation 2.26 we obtain:

$$I_s = \frac{R_\downarrow - R_\uparrow}{R_\uparrow + R_\downarrow} I = PI \tag{2.29}$$

The resistance in parallel to the current source is equal to $R_\uparrow + R_\downarrow$
The difference in chemical potential $\Delta\mu$ is given by

$$\Delta\mu = (R_\uparrow - R_\downarrow)I = P(R_\uparrow + R_\downarrow)I \tag{2.30}$$

Taking into account that $R_\uparrow \simeq R_\downarrow \simeq 2R_c$, with R_c the contact resistance we obtain:

$$\Delta\mu = 4R_c P I \tag{2.31}$$

Note that in our model derived in the previous section, we do not work with two spin channels but we use directly the difference $\Delta\mu = \mu_s$. The resistor model gives spin currents of:

$$\begin{aligned} j_s \mid_{(x=0)} &= \mu_s / 2R_c \\ j_s \mid_{(x\neq 0)} &= N_\uparrow D \frac{d\mu_s}{dx} W \end{aligned} \tag{2.32}$$

where W is the width of the nonmagnetic material and $N_\uparrow$ the density of states at the Fermi level for the spin-up species.

The relaxation model gives spin currents:

$$\begin{aligned} j_s \mid_{(x=0)} &= \mu_s / R \\ j_s \mid_{(x\neq 0)} &= \frac{d\mu_s}{dx} \end{aligned} \tag{2.33}$$

The resistor model and the spin relaxation model should give the same ratio $j_s \mid_{(x=0)} / j_s \mid_{(x\neq 0)}$, from this we obtain the relation:

$$R = D N_\uparrow W R_c = \frac{R_c W}{R_{sq}} \tag{2.34}$$

In an experiment we can measure the contact resistance R_c and the square resistance R_{sq} and since the width W of the system is fixed, we are able to calculate the precise value of R.

2.2 Spin relaxation

Here we present possible spin relaxation mechanisms in a nonmagnetic material, for example in a graphene layer or in a single wall nanotube. Spin relaxation in a nonmagnetic material is an unavoidable process which brings a non-equilibrium population of spins (found at the spin injector interface to the nonmagnetic system) into a uniform distribution over spin directions. We discuss three major mechanisms for spin relaxation in metals and semiconductors, the Elliott-Yafet, D'yakonov-Perel' and the hyperfine interaction [9].

2.2.1 Relaxation and dephasing time

The relaxation of a spin ensemble is described by the Bloch equations. When a external magnetic field is applied along the z-direction, the spins not only decay and diffuse but also precess:

$$\frac{\partial S_x}{\partial t} = \gamma(\vec{B}x\vec{S})_x - S_x/T_2 + D\nabla^2 S_x, \tag{2.35}$$

$$\frac{\partial S_y}{\partial t} = \gamma(\vec{B}x\vec{S})_y - S_y/T_2 + D\nabla^2 S_y, \tag{2.36}$$

$$\frac{\partial S_z}{\partial t} = \gamma(\vec{B}x\vec{S})_z - S_z/T_1 + D\nabla^2 S_z, \tag{2.37}$$

where D is the diffusion constant and γ=$\mu_B g/\hbar$ is the electron gyromagnetic ratio with μ_B the Bohr magneton and g the electronic g factor. The longitudinal relaxation time, T_1, is the time it takes for the longitudinal magnetization to reach equilibrium. The dephasing (transverse) time, T_2, is the time needed for an ensemble of transverse spins to lose their phase coherence. From all-electronic spin transport measurements, we can extract both quantities T_1 and T_2 separately. The longitudinal time T_1 is extracted from the exponential dependence (as a function of the electrode spacing) of the spin valve signal. In the spin precession measurements the magnetic field is pointing in the z-direction, perpendicular to the spin direction, and therefore the transversal spin relaxation time T_2 is relevant.

2.2.2 Spin-orbit interaction

As explained below, spin-orbit interaction plays a huge role in the Elliott-Yafet mechanism and the Dyakonov-Perel mechanism. Spin-orbit interaction takes place when a particle carries a spin, has a speed v in the relativistic regime and moves in a region having a finite electric field E. Under those conditions the particle feels an effective magnetic field having a magnitude B_{eff}=(v x E)/c, where c is the speed of light. The electric field can have different origins, examples are the electric field from the atomic nuclei and the electric field present in crystals lacking inversion symmetry.

Elliott-Yafet mechanism

Elliott found [9] that conduction electron spins can relax via ordinary momentum scattering from impurities, boundaries, and phonons if the lattice ions induce spin-orbit coupling in the system (Fig. 2.9). Spin-orbit interaction mixes spin up and spin down states and therefore the Bloch states (momentum eigenstates) are not eigenstates anymore. The result is that the longitudinal time, T_1, is

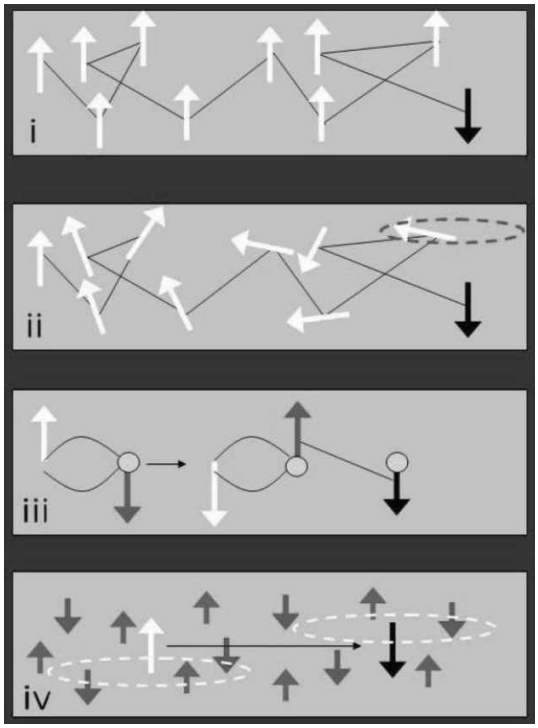

Figure 2.9: Four important mechanisms of spin relaxation in semiconductors (picture and figure caption taken from Fabian *et al.* [9]). From top to bottom: (i) The Elliott-Yafet mechanism, in which the electron scattering induced by impurities or phonons has a tiny chance to flip its spin at each scattering. (ii) The Dyakonov-Perel mechanism in which electron spins precess along a magnetic field which depends on the momentum. At each scattering the direction and the frequency of the precession changes randomly. (iii) The Bir-Aronov-Pikus mechanism, in which electrons exchange spins with holes (circles), which then lose spins very fast due to the Elliott-Yafet mechanism. (iv) If electrons wave functions (dashed circles) are confined over a certain region with many nuclear spins, the hyperfine coupling causes spin relaxation and dephasing.

proportional to the momentum scattering time, τ_p. Therefore, the spin flip length ($\lambda_{sf} = \sqrt{DT_1}$) is proportional to the mean free, since the diffusion constant is proportional to τ_p.

Dyakonov-Perel mechanism

In the Dyakonov-Perel mechanism [9] spin dephasing occurs because electrons feel an effective magnetic field, resulting from the lack of inversion symmetry and

from the spin-orbit interaction, which changes in random directions every time the electron scatters to a different momentum state (Fig. 2.9). The effective magnetic field has therefore a momentum dependency $\vec{B}(k)$. Spins precess with a Larmor frequency $\vec{\omega}(k) = e/m\vec{B}(k)$. The most important difference between the Elliott- Yafet and the Dyakonov-Perel mechanisms is their opposite dependence on the momentum scattering time. Strong scattering makes the Elliott-Yafet mechanism more effective and the Dyakonov-Perel processes less effective. This due to the fact that in the Elliott-Yafet process the loss of phase occurs only in the short time during collision. In the case of Dyakonov-Perel process, spin phases are randomized between collisions, since electrons precess with different frequencies depending on their momenta. Here, the spin relaxation time τ_{sf} is inversely proportional on the momentum scattering time. Experimentally we can make a distinction between the two mechanisms by investigating the dependence of their spin diffusion lengths λ_{sf}=$\sqrt{D\tau_{sf}}$ on momentum scattering τ_p. Since the diffusion constant is proportional to τ_p , for Elliott-Yafet $\lambda_{sf} \sim\tau_p$. In the case of Dyakonov-Perel mechanism the spin diffusion length does not depend on the momentum scattering time and for a degenerate electron system should be a constant independent of temperature.

For the Dyakonov-Perel mechanism the relation between the spin relaxation time and spin dephasing time can be obtained by comparing the following spin relaxation and dephasing rates [9]:

$$\frac{1}{T_1} = (< \omega_x^2 > + < \omega_y^2 >)\frac{\tau_c}{\omega_0^2\tau_c^2 + 1} \tag{2.38}$$

$$\frac{1}{T_{2x}} =< \omega_z^2 > \tau_c + < \omega_y^2 > \frac{\tau_c}{\omega_0^2\tau_c^2 + 1} \tag{2.39}$$

$$\frac{1}{T_{2y}} =< \omega_z^2 > \tau_c + < \omega_x^2 > \frac{\tau_c}{\omega_0^2\tau_c^2 + 1} \tag{2.40}$$

Here ω_0 is the frequency of spin precession for a magnetic field oriented along the z-direction (called Larmor frequency), $< \omega_x^2 >$, $< \omega_y^2 >$ and $< \omega_z^2 >$ are the expectation values of the precession frequency along the x, y and z axis. The random fluctuating field which the moving electron feels, has a correlation time, τ_c. The value of τ_c is determined by the momentum scattering relaxation time, τ_p. The dephasing time, T_2, is not necessary equal in the x and the y direction and therefore two components are given, T_{2x} and T_{2y}.

The relaxation and dephasing rates simplify for an isotropic material where $< \omega_x^2 >=< \omega_y^2 >=< \omega_z^2 >$ and therefore $T_{2x} = T_{2y}$. If the correlation time τ_c is small, such that $\omega_0\tau_c << 1$, the dephasing and the relaxation times become equal ($T_1 = T_2$). The spin transport experiments in graphene presented in chapters 6

to 8 are performed under the condition $\omega_0\tau_c << 1$ and measurement of T_1 and T_2 reveals that $T_1 \simeq T_2$, as expected.

Hyperfine interaction

The hyperfine interaction is the interaction between the magnetic moments of the electrons and the nuclear magnetic moment (Fig. 2.9). This mechanism dominates in the case of localized electrons, for example in quantum wells and quantum dots. There are two reasons why hyperfine interaction should be small in organic systems. First of all, for free electrons (holes) the interaction with the nuclei is weak and second, if natural carbon source is used, about 99% of the carbon atoms have no nuclear spin (N = 12).

2.3 Graphene

Graphene is a single layer of graphite, a honeycomb two-dimensional lattice of carbon atoms (see Fig. 2.10a). It has excellent material properties, namely it is thermally stable to temperatures up to 500 ^{o}C in air, inert to most gases, as strong as diamond, has a high mobility and a high current-carrying capacity. The graphite layer is only one-atom thick, therefore already one of the dimensions has reached its ultimate limit and enabling further miniaturization of electronics.

2.3.1 Graphene electronics

The properties of graphene have been studied theoretically for several decades already. However, only a few years ago it has became possible to isolate single graphene layers and to study their electronic properties experimentally [10, 11]. The unique graphene band structure (see Fig. 2.10 b) gives rise to new fascinating effects, such as anomalous quantum Hall effects [11]. In Fig. 2.10 b) the valence and conduction bands touch each other at six points and coincide with the corners of the hexagonal Brillouin zone. Graphene is therefore a semimetal (zero band gap semiconductor). Around the so-called Dirac neutrality points (K, K' in Fig. 2.10 b) the electronic states with energy E (relative to the Dirac point energy) can be described by a Dirac-like wave equation, with the velocity of light replaced by the Fermi velocity $v_F = 10^6$ m/s:

$$i\hbar v_F \begin{pmatrix} 0 & \partial_x - i\partial_y \\ \partial_x + i\partial_y & 0 \end{pmatrix} \begin{pmatrix} \Psi_A(r) \\ \Psi_B(r) \end{pmatrix} = E \begin{pmatrix} \Psi_A(r) \\ \Psi_B(r) \end{pmatrix} \tag{2.41}$$

where $\Psi_A(r)$ and $\Psi_B(r)$ describe the carrier wavefunction on the A and B sites

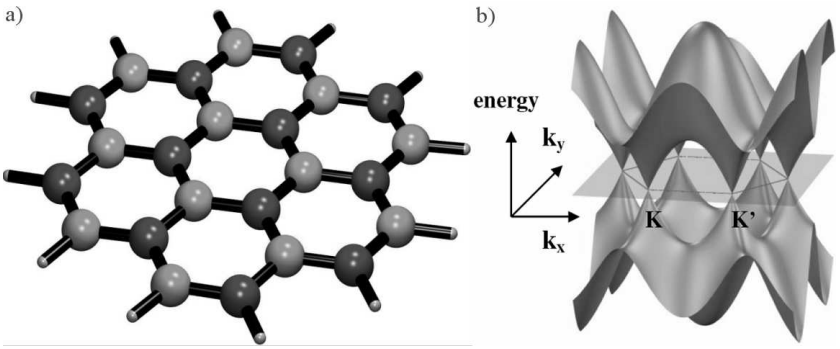

Figure 2.10: a) Graphene honeycomb lattice showing the two non-equivalent A (dark atoms) and B (light atoms) sublattices of carbon atoms. b) Graphene band structure (energy vs. carrier momentum in x and y direction) showing the nonequivalent K and K valleys. The other 4 valleys visible in the figure are equivalent to either K or K`, since they are separated by a reciprocal lattice vector. In the figure the Fermi energy (transparent plane) is located at the Dirac neutrality points, which separate the hole states below them from the electron states above them. The Fermi energy can be shifted up and down when the graphene carrier density is changed, e.g. with the use of electrostatic gating.

respectively at a position r (=x,y) in the graphene layer.

By applying a gate voltage we are able to tune the type of charge carriers in graphene, between electrons and holes with concentration n as high as 10^{13} cm^{-2} and a mobility, μ, which can exceed 2 10^5 cm^2 V^{-1} s^{-1} [12,13]. For the moment the mobility is limited by impurity and phonon scattering. In the samples used in our study we found mobilities in the range 2 - 4 10^3 cm^2 V^{-1} s^{-1} (Fig. 2.11). The semi-classical Drude model enables us to calculate the mobility μ:

$$\mu = \frac{\sigma}{en} \tag{2.42}$$

where e is the electron charge, n the charge density and σ the conductivity. This equation does not hold at and close to the Dirac point. The charge density can be extracted from the relation $n = \alpha(V_g - V_D)$ where, V$_g$ is the gate voltage, V$_D$ is the voltage at which the Dirac point (charge neutrality point) is found and $\alpha = 4.3\ 10^{10} cm^{-2} V^{-1}$ for a silicon oxide layer of 500 nm thickness.

Furthermore, another important quantity is the diffusion constant D, from which the scattering mean free path l ($= 2D/v_F$) can be calculated. We note that in order to calculate D from the Einstein relation $\sigma = e^2 \nu D$, we need to know σ which we measure experimentally, and the density of states $\nu(\varepsilon)$ which equals to:

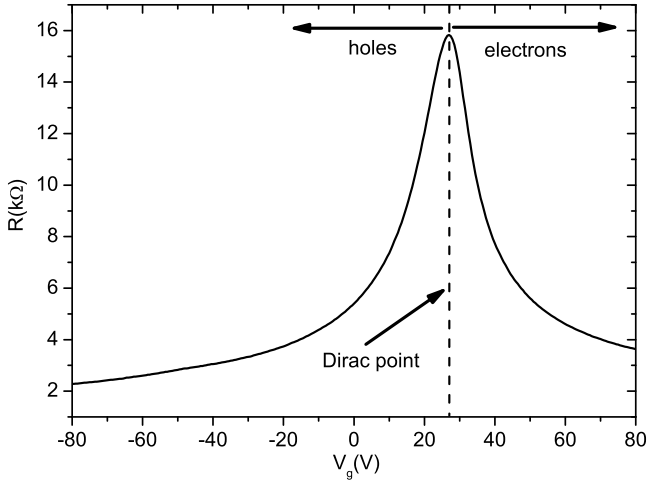

Figure 2.11: Resistance of a graphene layer (Sample A in chapter 7, length 5 μm, width 1.2 μm) as function of gate voltage V_g and at room temperature. Here a maximum resistance of 16 kΩ (3.8 kΩ resistivity) is found at V_g = 28 V. This maximum resistivity is found at the charge neutrality point, also known as Dirac point. Tuning the gate voltage to the right of the Dirac point induces electron charge carries into the graphene layer. Tuning V_g to the left induces holes into the system.

$$\nu(\varepsilon) = \frac{g_v g_s 2\pi \mid \varepsilon \mid}{h^2 v_F^2} \tag{2.43}$$

where the spin degeneracy gives $g_s = 2$ and the two-fold valley degeneracy $g_v = 2$ [14]. In the above equation ε is still unknown, but can be calculated from:

$$n(\varepsilon) = \frac{g_v g_s 2\pi \varepsilon^2}{h^2 v_F^2} \tag{2.44}$$

Since a graphene layer is not perfect but contains impurities and vacancies, the density of states at the Dirac point ($\varepsilon = 0$) is not zero but has a finite value. It can be approximated as:

$$\nu(\epsilon = 0) \approx 4\pi \frac{1}{h v_F l} \tag{2.45}$$

where l is the scattering length of the charge carriers. Using the Einstein

relation we obtain the diffusion constant at the Dirac point D = $\sigma/\nu e^2$. Unfortunately, the value of l is not known and therefore electronic measurements do not allow an exact measurement of the diffusion constant. However, a precise measurement of D can be obtained by performing a spin precession experiment. In chapter 6 we present spin precession measurements in graphene and measure the diffusion constant at the Dirac point. Performing the same experiment at high electron densities shows that the diffusion constant has a weak dependence in the charge density. From this we can also conclude that l does not change considerably as function of charge density in our samples.

2.3.2 Graphene spintronics

Theory predicts that spin life times in graphene should be relatively long [15–19]. Therefore, graphene could become a very good material for future spintronic devices. There are two reasons why spin relaxation time in graphene is expected to be long.

First, the weak hyperfine interaction between the electron spins and the nuclear spins. One of the reasons is that only about 1% of the carbon atoms consists of the isotope C13 , which carries a nuclear spin. Second, a weak spin-orbit interaction. Spin orbit interaction is a relativistic effect where the electric fields around the nuclei are seen by the moving electrons as a magnetic field, which can therefore give rise to a randomization of their spin directions, and thus effectively cause spin relaxation. Because of the low atomic number of carbon (Z = 6) this spin orbit interaction should be weak, since its strength scales with Z^4.

Experiments performed in our group [20] (Chapter 6) and in other groups [21–24] showed that spin injection, spin transport and spin manipulation in graphene at room temperature is possible. However, the spin relaxation times are found to be relatively short, of the order of 150 ps. Related to this it was found that the spin relaxation length, which is the length that a carrier in graphene can travel before loosing its initial spin direction, is about 1.5 μm.

Charge and Spin drift

In a diffusive system a charge carrier moving with the Fermi velocity v_F is subject to random scattering. Applying now an external electric field $\vec{E}$ gives to this random motion a small net velocity parallel (or antiparallel, depending on the type of charge carrier) to $\vec{E}$, which is called drift velocity $\vec{v}_d$ ($= \mu\vec{E}$). Since the mobility μ in graphene is high, a small electric field can result in large drift velocities, comparable to the Fermi velocity v_F. The proper way to calculate the drift velocity in graphene is to use the relation:

$$\vec{v}_d = \frac{\vec{j}}{ne} \tag{2.46}$$

where $\vec{j}$ is the current density, n the charge density and e the electron charge. Since the dispersion relation in graphene is given by $\epsilon(k) = \hbar v_F k$, it follows that the group velocity $\vec{v}_g(k)$ in graphene is a constant:

$$\vec{v}_g(k) = v_F \frac{\vec{k}}{\mid \vec{k} \mid} \tag{2.47}$$

Applying now an external electric field $\vec{E}$ results to a shift of the k-vectors by an amount $\Delta\vec{k} = e\vec{E}\tau/\hbar$, with τ the collision time of an electron (Fig. 2.12). The group velocity becomes:

$$\vec{v}_g(\vec{k} + \Delta\vec{k}) = v_F \frac{\vec{k} + \Delta\vec{k}}{\mid \vec{k} + \Delta\vec{k} \mid} \tag{2.48}$$

The current density can be calculated by integrating the carrier velocities in the two dimensional k-space:

$$\vec{j} = 2e \int_0^{k_F} \int_0^{2\pi} \frac{1}{(2\pi)^2} k \vec{v_g}(\vec{k} + \Delta\vec{k}) dk d\theta \tag{2.49}$$

The solution of the integrals is in the form of a Hypergeometric function and does not add any insight to the physics. An insightful solution can be obtained when calculating the current density for a small displacement in the $+\mathrm{k}_x$ direction (Fig. 2.12a). In this case the number of electronic states N contributing to the current flow is two times the number of electronic states found in the filled area in Fig. 2.12a. To calculate the number of electronic states in this filled area we use the approximation:

$$N(\theta, k) = cos(\theta)\nu(k)\Delta k \tag{2.50}$$

where $N(\theta, k)$ is the number of states as function of the angle θ (angle between the $+k_x$ axis and k). The density of states $\nu(k)$ is given by equation 2.43. $N(\theta, k)$ reaches its maximum value at $\theta = 0$, which are the states parallel to the k_x axis in Fig. 2.12. $N(\theta, k)$ becomes zero at $\theta = \pi/2$ (states parallel to k_y). The velocity u_x of a charge carrier in the k_x direction is approximately given by $cos(\theta)v_F$. The current density is then:

$$\vec{j} = 2 \int_0^{\pi/2} N(k) u_x d\theta = \frac{\pi\nu(k)e^2 v_F \tau E}{2\hbar} \tag{2.51}$$

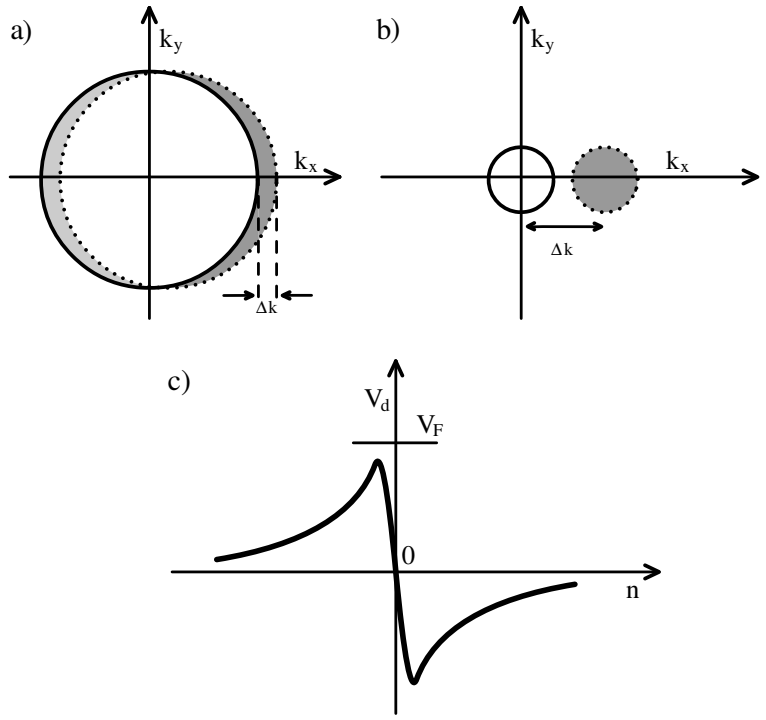

Figure 2.12: Charge drift. a) Application of an electric field E along the k_x direction shifts the Fermi surface to the right by $\Delta k = eE\tau/\hbar$. Only electrons in the filled area contribute to the current flow. b) Approaching the Dirac point results in a smaller Fermi surface. c) Drift velocity v_d as function of charge density n. If the collision time τ is independent of n then the drift velocity reaches the Fermi velocity just before $n = 0$.

From this we obtain a drift velocity

$$v_d = \frac{\sqrt{\pi} v_F e\tau}{\hbar\sqrt{2n}} E \tag{2.52}$$

Since the drift velocity in graphene can be large, we can manipulate the spin relaxation length in a graphene based spin valve device. We start with de steady state drift-diffusion equation [25] in terms of the spin imbalance $n_s = n_\uparrow - n_\downarrow$,

$$D\nabla^2 n_s + \vec{v}_d \vec{\nabla} n_s - \frac{n_s}{\tau_s} = 0 \tag{2.53}$$

where D is the diffusion constant and τ_s the spin relaxation time. Taking into account transport in the x-direction we obtain the general solution:

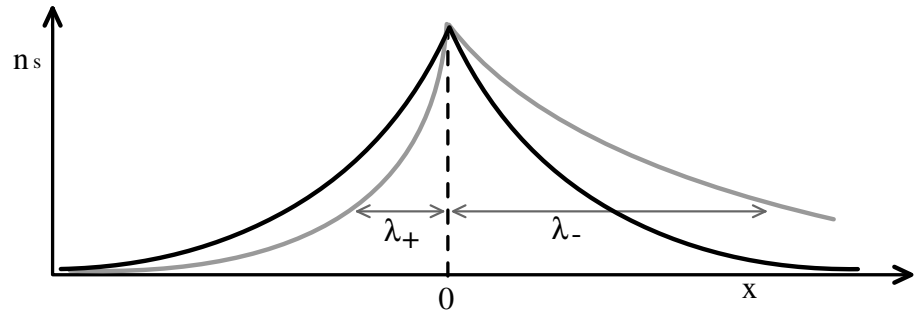

Figure 2.13: Spin density as function of the distance x from the spin source. *Black line*: Spins injected at x = 0 diffuse symmetrically, having a spin relaxation length λ_{sf}. *Gray line*: An electric field applied parallel to the x-direction induces drift to the spin carriers towards the right side. The combined effect of diffusion and drift results to an asymmetric spin relaxation, having a characteristic "upstream" relaxation length smaller than the "downstream" relaxation length ($\lambda_- > \lambda_+$)

$$n_s(x) = A\exp(+\frac{x}{\lambda_+}) + B\exp(-\frac{x}{\lambda_-}) \tag{2.54}$$

The prefactors A and B are determined by the boundary conditions and the relaxation lengths, $\lambda_\pm$, are given by:

$$\frac{1}{\lambda_\pm} = \pm\frac{1}{2}\frac{1}{\lambda_d} + \sqrt{\frac{1}{4}\frac{1}{\lambda_d^2} + \frac{1}{\lambda_{sf}^2}}. \tag{2.55}$$

Here, $\lambda_{sf} = \sqrt{D\tau_{sf}}$ is the spin diffusion length and $\lambda_d = D/v_d$ the spin drift length. In equation 2.55 the symmetric diffusion and asymmetric drift effects add up to form a spin transport characterized by a pair of length scales, named *upstream* and *downstream* lengths $\lambda_\pm$ (Fig. 2.13). In an experiment (Chapter 8), switching the electric field direction (along/against the spin transport direction) or changing the type of charge carriers (electrons/holes) by applying a gate voltage, allows us to control the spin relaxation length considerably. In one case (charge carriers: electrons, electric field: -E) the spins move "upstream", since the the spins need to travel against the action of the carrier drift to reach the spin detector, resulting to a reduction of the spin valve signal and of the spin relaxation length (λ_+). In the other case (charge carriers: electrons, electric field: +E) the spins move "downstream", resulting to an enhancement of the spin valve signal.

One last question to be answered is how the drift velocity v_d changes as function of the charge density n. Keeping the electric field E constant and reducing the charge density n from the metallic regime down to the charge neutrality point(n

= 0) can change the drift velocity considerably. If the collision time τ is independent of n then at sufficient small densities the drift velocity drastically increases and reaches the Fermi velocity (Fig. 2.12 c). At $n = 0$ the drift velocity becomes zero. However, if τ is proportional to $\sqrt{n}$ then the drift velocity remains constant at small charge densities and becomes zero at $n = 0$. Which of the two pictures holds for graphene is still not known.

2.4 Carbon nanotubes

A single-walled carbon nanotube can be formed by rolling up a graphene layer. Rolling up another graphene layer results in a double-walled nanotube. Repeating this procedure several times results to the so-called multiwalled carbon nanotube. Carbon nanotubes belong to the fullerene family, which also includes the C_{60} buckyball molecule. First reports of multiwalled nanotubes are from Radushkevich and Lukyanovich in 1952 [26] and about 40 years later from Iijima [27, 28]. The discovery of single wall nanotubes in 1993 was done by accident when scientists tried to fill multiwalled nanotubes with metals [29, 30]. The metals instead of filling the nanotube, worked as catalytic particles for the creation of single wall nanotubes.

In our experiments we used single wall carbon nanotubes. The diameter of each nanotube is measured with an atomic force microscope. The diameter of a single walled carbon nanotube can be as small as 0.6 nm and as large as 3 nm. Depending on the chirality of the nanotube it can have metallic or semiconducting electronic properties [31].

2.4.1 Carbon nanotube electronics and spintronics

The electronic properties of a SWNT strongly depends on how the graphene sheet is wrapped up [31]. A pair of indices (n,m) which is called the chiral vector characterizes each nanotube. The integers n and m denote the number of unit vectors along two directions in the honeycomb crystal lattice of graphene (Fig. 2.14) There are thee types of nanotubes, zigzag, armchair and chiral. Zigzag SWNT's have $m = 0$, armchair $n = m$ and all other combinations of n and m are chiral. In general, a nanotube is metallic if n - m is a multiple number of 3. An armchair nanotube is therefore metallic. Nanotubes are semiconducting in all other cases. Interestingly, the energy gap scales with the tube diameter as 1/d and is of the order of 0.5 eV for a SWNT with typical diameter d = 1.4 nm. Electronically, a metallic carbon nanotube is superior to any other known inorganic conducting material, since it can survive electrical current densities as

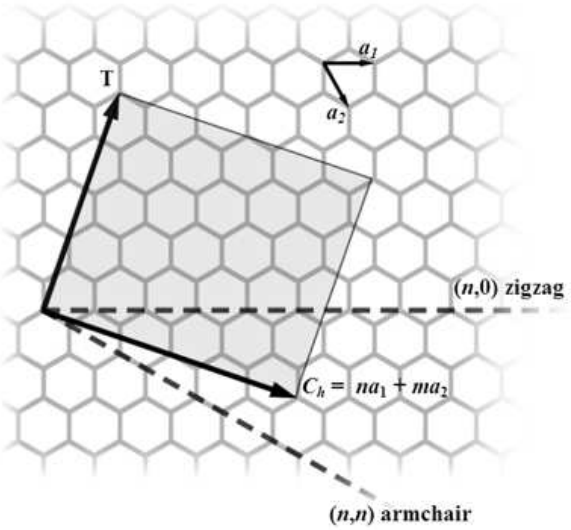

Figure 2.14: The (n,m) nanotube naming scheme can be thought of as a vector (C_h) in an infinite graphene sheet that describes how to "roll up" the graphene sheet to make the nanotube. T denotes the tube axis, and a_1 and a_2 are the unit vectors of graphene in real space.

high as 1 TAcm^{-2}, 1000 times larger than the densities in metals such as silver and copper.

For the same reasons as graphene, carbon nanotubes are expected to be good candidates for spintronic devices. The first organic spintronic device was reported by Tsukagoshi *et al* in 1999 [32], and remarkably, it consisted of a multi-walled carbon nanotube contacted by Co contacts. Many other spintronic experiments on multi- and single-walled carbon nanotubes followed up. Unfortunately, the experiment of Tsukagoshi and all other experiments performed after his work have made use of the conventional two-terminal spin valve geometry [33–39]. The use of this geometry makes it difficult to separate spin transport from other effects, such as Hall effects, anisotropic magnetoresistance [2, 3], interference effects [4] and magneto-coulomb effects [5]. These may obscure and even mimic the spin accumulation signal. In chapter 4 we present spin transport in a single wall nanotube using a four-terminal non-local spin valve geometry [2, 6, 7]. Here, one is able to completely separate the spin current path from the charge current path. Hence, the signal measured is due to spin transport only.

References

[1] E. P. Wohlfarth, *Ferromagnetic materials* (North Holland, 1982), chap. 9, review article *Transport properties of ferromagnets*, I. A. Campbell, A. Fert, p. 747

[2] F.J. Jedema, A. T. Filip and B. J. van Wees, *Nature* **410**, 345 (2001).

[3] B.W. Alphenaar, S. Chakraborty and K. Tsukagoshi, in *Electron Transport in Quantum Dots* (Kluwer Academic/Plenum Publishers, New York 2003) chap. 11.

[4] H.T. Man and A.F. Morpurgo, *Phys. Rev. Lett.* **95**, 026801 (2005)

[5] K. Ono, H. Shimada and Y. Ootuka, *J. Phys. Soc. Jpn* **67**, 2852 (1998); H. Shimada, K. Ono, and Y. Ootuka, *J. Appl. Phys.* **93**(10), 8259 (2003)

[6] M. Johnson and R.H. Silsbee, *Phys. Rev. Lett.* **55**, 1790 (1985)

[7] F.J. Jedema *et al.*, *Nature* **416**, 713 (2002)

[8] G. Schmidt, *et al.*, *Phys. Rev. B* **62** R4790 (2000)

[9] I. Zutic, J. Fabian and S. Das Sarma, *Reviews of Modern Physics* **76**, (2004)

[10] A.K Geim and K.S. Novoselov, *Nature Materials* **6**, 183 (2007)

[11] Y. Zhang, *et al.*, *Nature* **438**, 201 (2005)

[12] K. I. Bolotin, *et al.*, cond-mat/0802.2389v1 (2008)

[13] S.V. Morozov, *et al.*, *Phys. Rev. Lett.* **100**, 016602 (2008)

[14] T. Ando, *J. Phys. Soc. Japan* **75**, 074716 (2006)

[15] C.L. Kane and E.J. Mele, *Phys. Rev. Lett.* **95** (2005)

[16] Y. Yao *et al.*, cond-mat/06063503

[17] Honki Min *et al.*, *Phys. Rev. B* **74**, 165310 (2006)

[18] D. Huertas-Hernando, F. Guinea, and A. Brataas, *Phys. Rev. B* **74**, 155426 (2006)

[19] B. Trauzettel, D.V. Loss, and G. Burkard, *Nature Physics* **3**, 192 (2007)

[20] N. Tombros *et al.*, *Nature* **448**, 571 (2007)

[21] E.W. Hill, A.K. Geim, *et al.*, *IEEE Trans. Magn.* **42** (10) 2694 (2006)

[22] S. Cho, Y.F. Chen, and M.S. Fuhrer, *Appl. Phys. Lett.* **91**, 123105 (2007)

[23] M. Nishioka and A.M. Goldman, *Appl. Phys. Lett.* **90**, 252505 (2007)

[24] M. Ohishi et al., *Jpn. J. Appl. Phys.* Vol. **46**, No. 25 (2007)

[25] Z. G. Yu and M. E. Flatte, *Phys. Rev. B* **66**, 201202(R)(2002)

[26] M. Monthioux and V. L. Kuznetsov, *CARBON* **44**, 1621 (2006)

[27] S. Iijima, *Nature* **354**, 568 (1991)

[28] L. V. Radushkevich , V. M. Lukyanovich, *Zurn Fisic Chim* **26**, 88-95 (1952)

[29] S. Iijama, *Nature* **363**: 603 - 605 (1993)

[30] D. S. Bethune *et al. Nature* **363**, 605607 (1993)

[31] H. Dai, *Surface Science* **500**, 218241,(2002)

[32] K. Tsukagoshi, B. W. Alphenaar and H. Ago, *Nature* **401** 572 (1999).

[33] K. Tsukagoshi and B. W. Alphenaar, *Superlattices and Microstructures* **27**, 565 (2000).

[34] J. R. Kim *et al.*, *Phys. Rev. B.* **66**, 233401 (2002).

[35] S. Chakraborty *et al.*, *Appl. Phys. Lett* **83**, 1008 (2003).

[36] D. Orgassa, G. J. Mankey and H. Fujiwara, *Nanotechnology* **12**, 281 (2001).

[37] B. Zhao *et al.*, *J. Appl. Phys.* **91**, 7026 (2002)

[38] S. Sahoo, *et al.*, *Appl. Phys. Lett.* **86**, 112109 (2005)

[39] A. Jensen, thesis, Technical University of Denmark and University of Copenhagen, Copenhagen, Denmark (2003)